Title

Nanoporous Gold Biointerfaces: Modifying Nanostructure to Control Neural Cell Coverage and Enhance Electrophysiological Recording Performance

Journal

Advanced Functional Materials, 27(3)

ISSN

1616-301X

Authors

Chapman, Christopher AR
Wang, Ling
Chen, Hao
et al.

Publication Date

2017

DOI

10.1002/adfm.201604631

Peer reviewed

FULL PAPER

Nanoporous Gold Biointerfaces: Modifying Nanostructure to Control Neural Cell Coverage and Enhance Electrophysiological Recording Performance

*Christopher A. R. Chapman, Ling Wang, Hao Chen, Joshua Garrison, Pamela J. Lein, and Erkin Seker**

Nanostructured neural interface coatings have significantly enhanced recording fidelity in both implantable and in vitro devices. As such, nanoporous gold (np-Au) has shown promise as a multifunctional neural interface coating due, in part, to its ability to promote nanostructure-mediated reduction in astrocytic surface coverage while not affecting neuronal coverage. The goal of this study is to provide insight into the mechanisms by which the np-Au nanostructure drives the differential response of neurons versus astrocytes in an in vitro model. Utilizing microfabricated libraries that display varying feature sizes of np-Au, it is demonstrated that np-Au influences neural cell coverage through modulating focal adhesion formation in a feature size-dependent manner. The results here show that surfaces with small (≈30 nm) features control astrocyte spreading through inhibition of focal adhesion formation, while surfaces with large (≈170 nm and greater) features control astrocyte spreading through other mechanotransduction mechanisms. This cellular response combined with lower electrical impedance of np-Au electrodes significantly enhances the fidelity and stability of electrophysiological recordings from cortical neuron-glia co-cultures relative to smooth gold electrodes. Finally, by leveraging the effect of nanostructure on neuronal versus glial cell attachment, the use of laser-based nanostructure modulation is demonstrated for selectively patterning neurons with micrometer spatial resolution.

1. Introduction

Approaches for controlling cellular coupling to biomaterials have been an important research pursuit for advanced biointerfaces, where underlying mechanisms of cellular adhesion and reactivity to surfaces play an essential role.[1–3] Many cell types display altered structure and adhesion motifs as a function of material properties.[4] These properties, such as substrate stiffness, surface chemistry, and material structure (at both the micro- and nano-scale) offer potential parameters for controlling cell–material coupling without intervention from chemical cues such as pharmaceuticals. Therefore, a significant research effort has been devoted to controlling cell fate (e.g., phenotypic changes, adhesion, migration) by manipulating purely mechanical cues from substrate surfaces.[5–7] Although much of the research in this field has been directed toward controlling stem cell fate and differentiation by varying substrate stiffness and material nanostructure,[8–10] using mechanical cues to drive neural cell coupling presents an attractive means to improve the signal fidelity of neural interfaces.[11–14] Moving toward the development of neural recording interfaces with high fidelity and long-term stability requires an electrode interface that maintains close physical coupling between neurons and the electrode surface. However, an important obstacle in maintaining this close coupling is the coverage of the electrode surface by reactive glia via a process known as astrogliosis.[15,16] The accumulation of astrocytes during astrogliosis pushes neurons away from the electrode surface, decreasing electrical coupling and leading to reduced recording fidelity.[17] Although an acute immune response to the implanted devices is inevitable, designing neural interface materials that selectively promote neuronal surface coverage has the potential to significantly reduce the distancing of neurons from the electrode surface as a result of astrogliosis.

To date, many nanostructured materials have been successfully used as neural interface materials;[18–22] however, the signal-to-noise ratio gains seen on these materials are primarily due to reduced electrode impedance stemming from increased surface area-to-volume ratio of the electrodes.[23] Few

C. A. R. Chapman
Department of Biomedical Engineering
University of California, Davis
Davis, CA 95616, USA
Dr. L. Wang, J. Garrison, Prof. E. Seker
Department of Electrical and Computer Engineering
University of California, Davis
Davis, CA 95616, USA
E-mail: eseker@ucdavis.edu
H. Chen, Prof. P. J. Lein
Department of Molecular Biosciences
University of California, Davis
Davis, CA 95616, USA

DOI: 10.1002/adfm.201604631

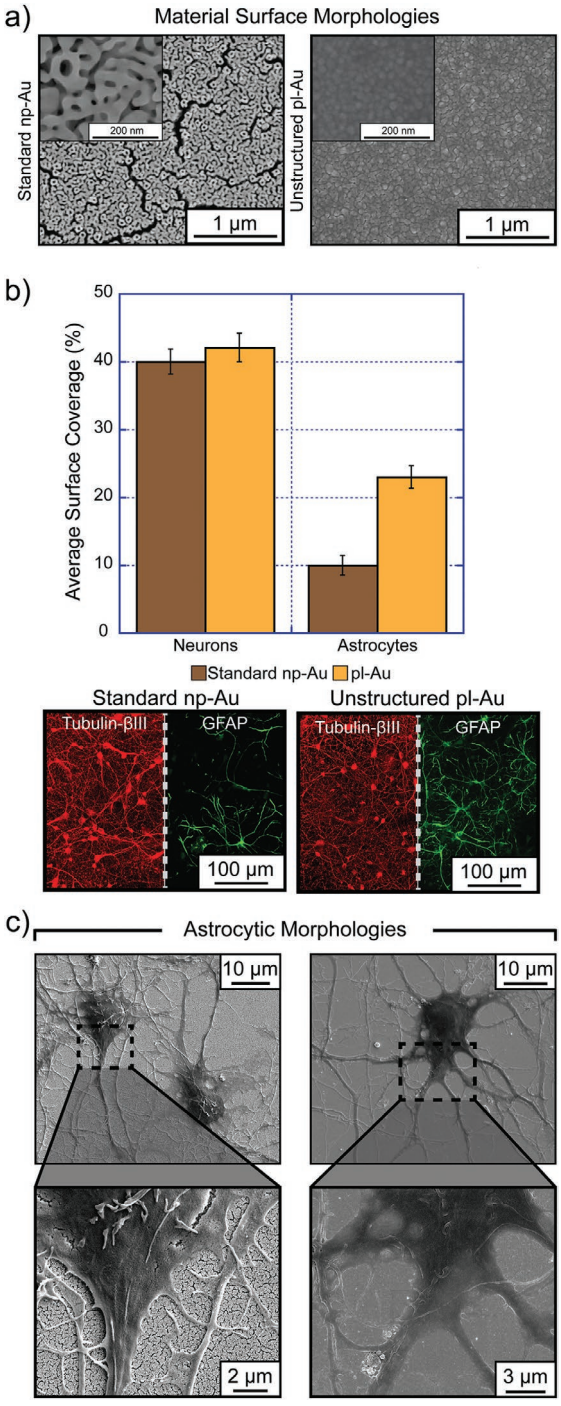

Figure 1. a) Scanning electron microscopy images of both standard np-Au (left) and pl-Au (right) show differences in material surface morphologies at low and high magnification. b) (Top) Surface coverage analysis of cortical neuron-astrocyte mixed cultures grown on standard np-Au and pl-Au demonstrate the reduction in astrocyte coverage that is seen on the np-Au substrate. (Bottom) Fluorescence microscopy images of neuron-specific tubulin-βIII immunoreactivity and astrocyte-specific GFAP immunoreactivity on both standard np-Au and pl-Au demonstrate the significant reduction in astrocytic surface coverage seen on np-Au. c) Low- and high-magnification scanning electron microscopy images of astrocytes on np-Au (left) and pl-Au (right) illustrate the differences in process growth between astrocytes on these surfaces.

of these materials have reported an ability to effectively use nanostructure to selectively control the adhesion of neurons versus astrocytes.[24] An emerging nanostructured material that has shown promise as a neural interface due to low impedance and a selective reduction in astrocytic surface coverage is nanoporous gold (np-Au).[25–27] Np-Au is composed of a network of gold pores and ligaments that are created by selective dissolution of silver from a gold-silver alloy.[28] We have previously reported that np-Au films with an average ligament width of 30.6 ± 1.2 nm and average pore diameter of 87.11 ± 4.55 nm, the standard np-Au morphology used in our lab and denoted as "standard np-Au" in this paper (**Figure 1**a), have been shown to selectively reduce astrocyte surface coverage by 50%–60% while maintaining neuronal surface coverage at levels similar to unstructured planar gold (pl-Au) surfaces (Figure 1b). Although the mechanism responsible for this specific reduction in surface coverage was linked to mechanical cues from np-Au surface morphology,[27] the underlying cellular mechanisms that drive this process are not fully understood. Here, we report possible cellular mechanisms involved in selectively reducing astrocytic surface coverage on np-Au surfaces. Due to the differences in astrocytic morphology captured via immunostaining (Figure S1, Supporting Information), we have previously hypothesized that the np-Au surface morphology controls astrocyte spreading by hindering the formation of focal adhesion complexes necessary for spreading of cellular processes. Using a primary cortical neuron-astrocyte co-culture model, we probed focal adhesion formation as a function of both culture duration and material (i.e., unstructured and nanostructured gold). Additionally, utilizing on-chip libraries of multiple np-Au morphologies fabricated through a laser-based photothermal annealing process,[29] the nanostructure dependence of the focal adhesion assembly response was investigated. Through these studies, we were able to demonstrate significant differences in the assembly of astrocytic focal adhesions as a function of material nanostructure and to identify multiple ways in which feature size controls how astrocytes react to the np-Au surface. Finally, we demonstrated the influence of this cell–material interaction on electrophysiological recordings and further leveraged the nanostructure-driven differential cell attachment to pattern neurons with high spatial resolution.

2. Results and Discussion

In order to more closely visualize the micro- and nano-sized interactions of astrocytes on material surfaces, we acquired scanning electron microscopy images of astrocytes from day in vitro (DIV) 3 cortical co-cultures plated on either standard np-Au or pl-Au surfaces. Astrocytes were discriminated from neurons (and fibroblasts) by their distinct reactive star-like morphology, large processes, and specific cell body height that is flatter than neurons but higher than fibroblasts (Figure S2, Supporting Information).[30] Striking differences in astrocyte morphology between cultures grown on standard np-Au and pl-Au surfaces confirmed the morphological differences previously documented by immunofluorescence microscopy (Figure 1c).

2.1. Focal Adhesion Formation on np-Au Surfaces

To quantify the effect of np-Au nanostructure on the formation of astrocytic focal adhesions, we quantified vinculin expression at focal adhesion sites.[31,32] Since cellular surface interactions are extremely mechanosensitive with even nanoscale level changes in feature sizes exerting significant influence on the adhesive behavior of many of cell types,[8,33,34] it is necessary to study a wide range of feature sizes to effectively investigate nanostructure-dependent responses. To that end, miniature libraries of varying np-Au topographies were created using photolithographic pattern transfer and photothermal annealing processes previously reported by our group.[29] These libraries on a single microfabricated chip allow for the simultaneous study of cell behavior on a wide range of feature sizes in a single culture well, which significantly increases throughput and reduces variations due to cell seeding and source. Here, we investigated focal adhesion formation on np-Au material libraries consisting of an array of three 9 mm^2 patterns. These patterns were annealed to three different morphologies corresponding to a wide range of feature sizes (**Figure 2**a). Morphology 1 (M1), which has the same ligament width as standard np-Au (30.6 ± 1.2 nm) but lacks surface cracking; Morphology 2 (M2), annealed to a ligament width of 176.6 ± 13.5 nm; and Morphology 3 (M3), annealed to a ligament width of 344.7 ± 26.1 nm.

Cortical neuron-astrocyte co-cultures were plated on all surfaces and then immunostained for both f-actin (cytoskeleton) and vinculin (focal adhesion) at either DIV 1 or 3. Fluorescent images of immunostained cells were used to quantify astrocyte shape and the underlying focal adhesion formation of the cells for the entire range of surface morphologies in our feature size libraries (Figure 2b). Astrocytes were differentiated from neurons based on differences in the cytoskeleton and isolated to analyze focal adhesion contact area and number of focal adhesions per astrocyte (Figure S3, Supporting Information), two properties that have been closely linked to cell spreading.[35,36]

Significant changes in focal adhesion contact area were observed between surface morphologies. Although the total focal adhesion contact area (Figure 2c) increased on each material over the 2 d period, it reached the highest value on pl-Au at 404.3 μm^2 per cell. At DIV 3 total focal adhesion contact area was significantly reduced on all np-Au morphologies. In comparison to pl-Au, a 1.3-fold decrease was observed on standard np-Au ($p < 0.01$), a 1.5-fold decrease on Morphology 1 ($p < 0.01$), a 2.1-fold decrease on Morphology 2 ($p < 0.001$), and finally a 7.1-fold decrease on Morphology 3 ($p < 0.001$). Although total focal adhesion contact area was significantly reduced on all np-Au morphologies at DIV 3, only astrocytes on Morphology 1 and standard np-Au showed significant changes in focal adhesion number in comparison to pl-Au at DIV 3, with increases of 3.2-fold and 1.9-fold ($p < 0.001$), respectively. This suggests that the comparable feature sizes of these two surfaces elicit a similar response from the astrocytes (i.e., a decrease in total focal adhesion contact area with an increase in focal adhesion number). The differences in the values between these two morphologies are likely due to the presence of large cracks on the standard np-Au surface (a result of the patterning process used to fabricate the standard np-Au). It is likely that these cracks are the driving force in the higher contact area and lower focal adhesion number seen in astrocytes on the standard np-Au surfaces. Ultimately the small np-Au nanostructure seems to arrest astrocyte attachment by requiring more focal adhesions to successfully attach to the material surface.

Here, we have identified changes in astrocyte focal adhesion formation in response to different nanoscale feature sizes of the surface morphology. The small feature sizes of Morphology 1 and standard np-Au (30.6 ± 1.2 nm) appear to be limiting the area of focal adhesion complexes, thus resulting in an increase in focal adhesion number ultimately leading to decreased cell stability and spreading over the material surface. This result is in line with previous findings suggesting that stable assembly of focal adhesions depends primarily on the area of focal adhesion clusters and not directly on the number of focal adhesions.[37,38] However, as feature size increases to ≈170 nm (Morphology 2), this effect becomes less pronounced as evidenced by less change in contact area and no increase in focal adhesion number per astrocytes relative to pl-Au. Feature sizes of ≈350 nm (Morphology 3) cause a further decrease in focal adhesion contact area with no increase in focal adhesion number, suggesting a potential shift in mechanism away from focal adhesion destabilization and toward a mechanism driven primarily by a decrease in focal adhesion area.

2.2. Driving Differential Neural Cell Coverage through Leveraging Focal Adhesion–Material Interaction

Although we have shown that astrocyte focal adhesion formation depends on the underlying substrate nanostructure, ultimately the goal is to control differential neural cell coverage (i.e., promote and/or maintain high neuron coverage while reducing or minimizing astrocyte coverage) using mechanical cues from the material surface. This necessitates investigation of how this relationship translates into surface coverage of astrocytes, as well as neurons, on each of the different material nanostructure sizes. Using neuron and astrocyte specific markers, the total surface coverage of both cell populations was quantified on standard np-Au patterns and np-Au material libraries presenting the same morphologies as described above (**Figure 3**).

Surface coverage analysis of neurons (**Figure 4**a) and astrocytes (Figure 4b) on each material revealed differences, that point toward the underlying mechanisms driving cell spreading being altered due to surface feature size. On Morphology 1 both astrocyte and neuron coverage decrease at both DIV 3 and 7; however, on standard np-Au, Morphology 2, and Morphology 3, the desired response of high neuronal coverage with reduced astrocyte coverage is maintained (especially at DIV 7). In agreement with the results previously seen on pl-Au, the differential reduction in astrocyte coverage is no longer observed on unstructured silicon. The small continuous feature size (≈30 nm) of Morphology 1 appears to be completely inhibiting cell attachment and subsequent spreading by decreasing the area of individual focal adhesion complexes. Interestingly, standard np-Au, which exhibits the same feature size albeit with large surface cracks, decreases astrocytic coverage without affecting neuronal coverage. It is plausible that neuronal surface coverage is not affected at DIV 7 on

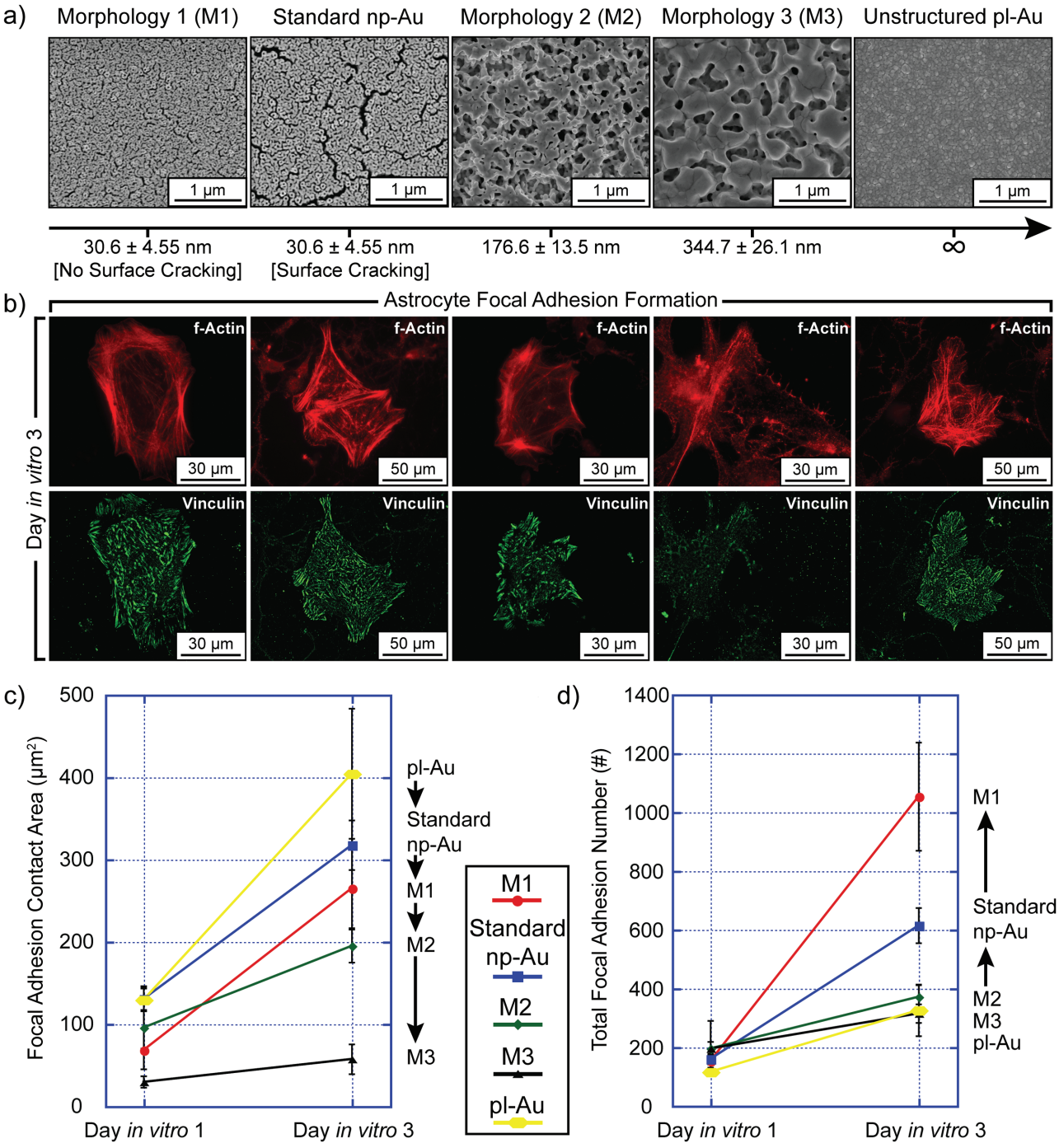

Figure 2. a) Scanning electron microscopy images of the morphology of the various gold surface morphologies tested starting with the smallest (left) and ending with the largest (right) feature size. Planar gold is considered to be an infinitely big feature size, in which cellular interactions with the surface are based solely on the material. b) The fluorescence microscopy images of the spatial patterns of f-actin immunoreactivity (red) and vinculin immunoreactivity (green) of cortical neuron-astrocyte co-cultures grown on the respective surfaces at DIV 3. c) The average total contact area of the focal adhesions as determined by vinculin immunoreactivity shows differences between all surface morphologies, with a reduction in total area from that of pl-Au. d) The average total number of focal adhesions per astrocyte on various morphologies demonstrates that the small feature size of Morphology 1 and standard np-Au significantly increases the total number of focal adhesions per cell, whereas the larger morphologies (2 and 3) result in no change in the number of focal adhesions relative to pl-Au.

standard np-Au because the area of the surface crack edges enables the formation of the neuronal point contacts needed for successful attachment and spreading. This is likely due to neuronal point contacts being smaller than astrocyte focal adhesion complexes[39] and thus requiring less surface area to support the spreading of neuronal processes across material

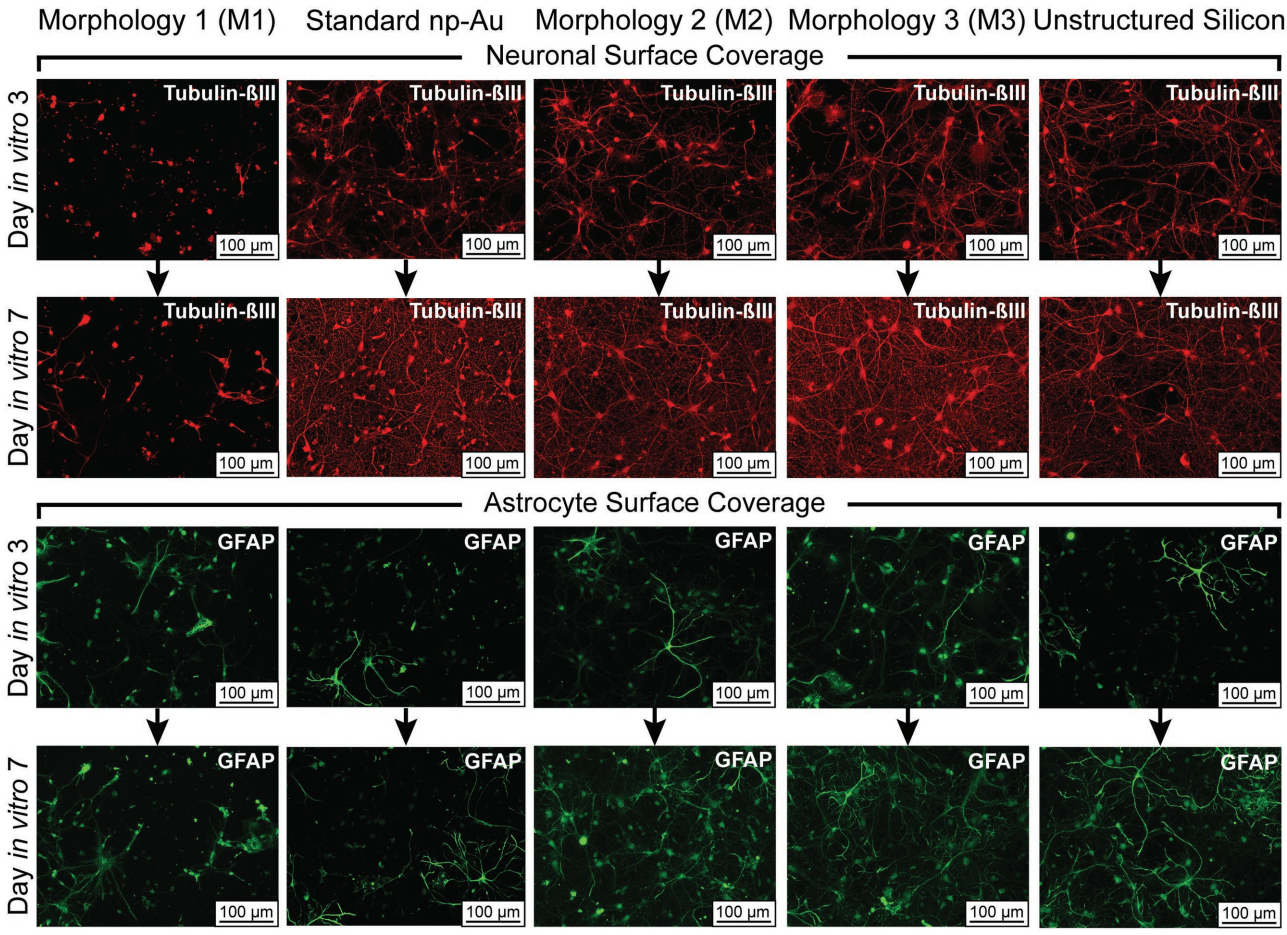

Figure 3. Fluorescence microscopy images illustrating differences in neuron versus astrocyte surface coverage of cortical neuron-astrocyte co-cultures on different surface morphologies. Neuron surface coverage was visualized using tubulin-βIII immunoreactivity (top, red); astrocyte surface coverage, GFAP immunoreactivity (bottom, green).

surfaces. Thus, the presence of surface cracking allows neurons to attach and spread adequately over the standard np-Au surface.[40,41] This suggests that small feature sizes (at least around 30 nm) are a critical factor in reducing cell spreading by limiting focal adhesion formation, which results in physically arrested cells.

On Morphology 2 and Morphology 3, where the np-Au films present much larger feature sizes, a reduced astrocytic surface coverage was also seen, which is consistent with our previous investigation.[27] Interestingly, contrary to the comparison between Morphology 1 and standard np-Au (where the presence of surface cracking in standard np-Au allows for an increase focal adhesion area) the total focal adhesion area does not increase due to larger feature sizes being present. Instead, there is a marked decrease in total focal adhesion area (Figure 4c) as the feature size increases from 30 nm to hundreds of nanometers. These observations suggest that the underlying mechanism(s) leading to the reduced astrocyte coverage changes from inhibition of stable focal adhesion complexes to other mechanotransduction mechanisms. Neurons and astrocytes demonstrate sensitivity to nanostructure through many pathways, such as the activation of integrin and/or YAP/TAZ-mediated pathways, and are not solely reliant on the formation of focal adhesion complexes.[11–13,16,42–44]

Plotting both neuronal and astrocyte surface coverage at DIV 3 with respect to the total focal adhesion contact area (Figure 4c) and total adhesion number (Figure 4d) highlights the shift in the mechanism from inhibition of focal adhesion formation due to small feature sizes, to reducing adhesion contact area in response to feature sizes larger than 170 nm. Although the results strongly suggest a change in the dominant mechanism controlling cell adhesion on these morphologies, identification of the specific driving factors requires further research. One potential factor may be differences in neural cell adhesion strength. Focal adhesion area has been closely tied to adhesion strength;[45] however, cell-specific adhesion strength may be playing an important role in the specific response to changing np-Au feature size. Additionally, future studies into the differences in gene expression between astrocytes (and neurons) on these differing feature sizes should provide more insight into the pathways and the complex reaction of neural cells to these nanostructured gold surfaces. These data are crucial both for controlling cell type-specific surface coverage as well as broadening the general understanding of cellular mechanotransduction in the brain.

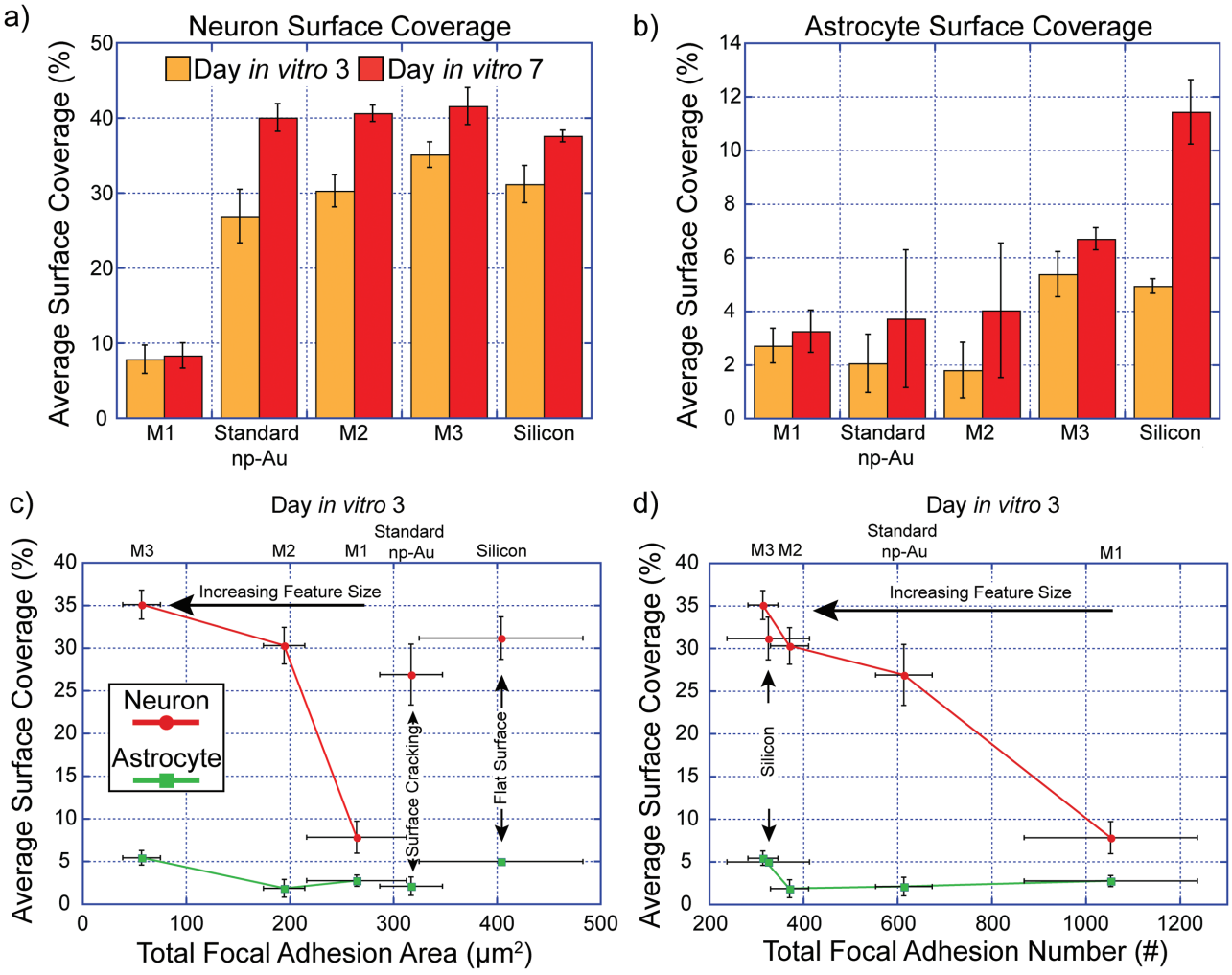

Figure 4. Comparison of average a) neuronal and b) astrocyte surface coverage on each feature size provides further insight into the effect of np-Au feature size on cell type-specific surface coverage. Astrocyte coverage remains reduced relative to neuronal coverage on all np-Au morphologies although this effect is potentially mediated by different mechanisms. Subsequently, comparison between surface coverage at DIV 3 versus the c) total focal adhesion area and d) total focal adhesion number suggests that the cracks in standard np-Au enable neuronal spreading over the surface while still reducing astrocytic surface coverage through an inhibition of focal adhesion size (leading to higher number of focal adhesions on these surfaces), whereas the surface coverage of astrocytes remains reduced on Morphology 2 and 3 through a shift toward different mechanisms (error bars represent standard error).

2.3. Effect of Nanostructural Cues on Electrophysiological Recording Performance

The ultimate goal of utilizing np-Au as an electrode interface is to improve both short- and long-term performance of recording electrodes. In order to investigate the direct effect of np-Au morphologies on long-term electrophysiological recordings, multiple electrode arrays consisting of 24 np-Au electrodes and 8 pl-Au control electrodes were fabricated with both the standard np-Au morphology and Morphology 3 (**Figure 5**a). The same primary cortical neuron-glia co-culture model used for the previous focal adhesion studies was maintained on the electrode arrays for 28 d in vitro, and both impedance and electrophysiological recordings were taken at specific time-points. Impedance analysis demonstrates that, even under culture conditions containing highly biofouling serum proteins, both morphologies of np-Au exhibited a consistently lower electrical impedance in comparison to pl-Au (Figure 5b). Specifically, the impedance values at 1 kHz demonstrated a sustained 5-fold decrease for standard np-Au and threefold decrease for Morphology 3 electrodes. While the lowered electrical impedance is due to augmented surface area-to-volume ratio,[23,25] the electrical stability of the np-Au electrodes in biofouling conditions is attributed to the nanoporous network sieving out large proteins while allowing transport of ions and small molecules, as previously reported.[46,47] As a result of impedance values that are lower than pl-Au, both np-Au morphologies exhibited significantly lower background noise in comparison to the pl-Au electrodes (Figure 5c). Signal analysis of electrophysiological recordings at days in vitro 7, 14, 21, 25, and 28 also reveal significant differences between the three different electrode morphologies. Although both np-Au morphologies exhibited

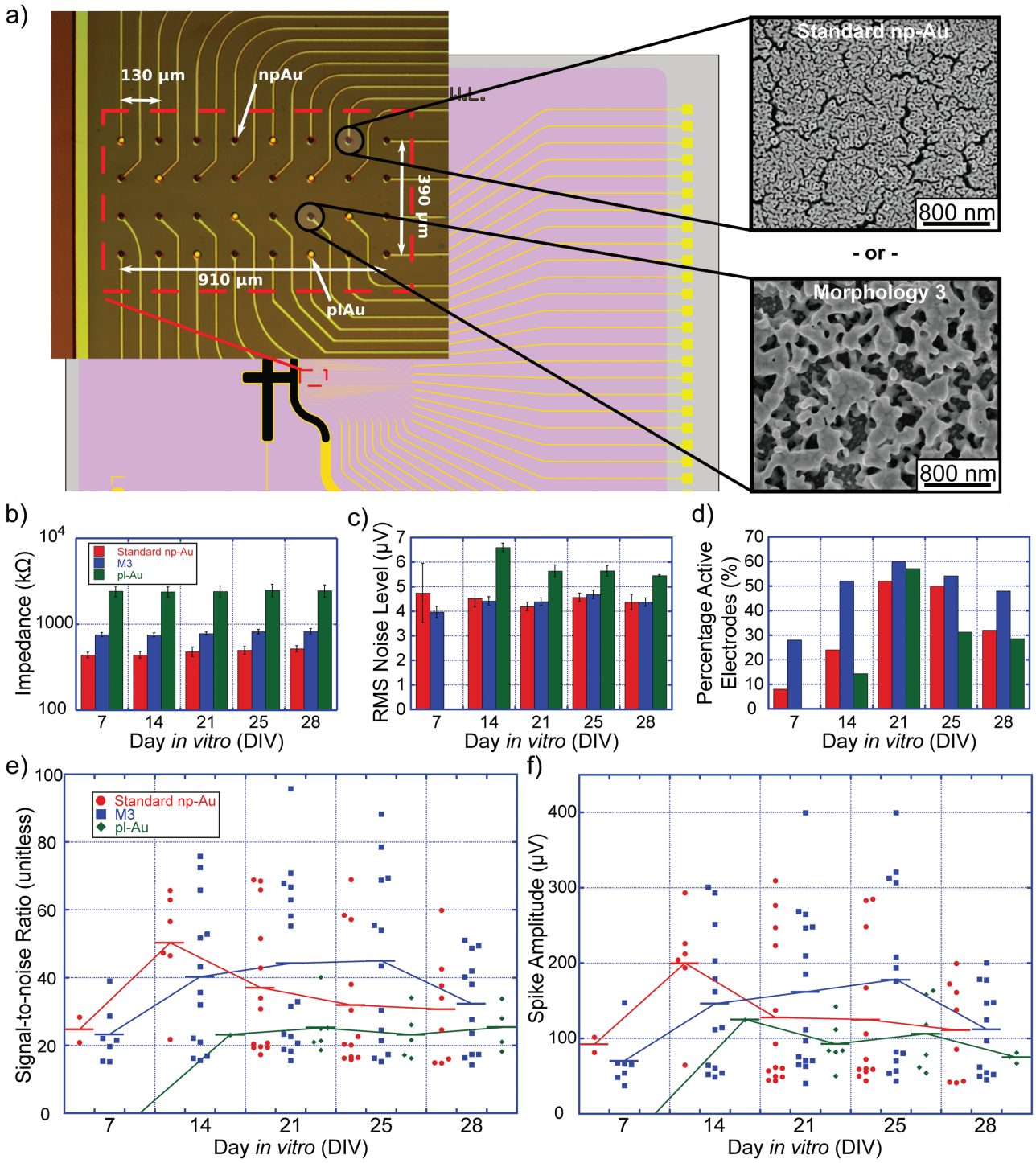

Figure 5. a) Microfabricated multiple electrode arrays (MEAs) consisted of 28 standard np-Au electrodes (20 µm in diameter) and 8 pl-Au electrodes. One MEA was thermally annealed to create electrodes with Morphology 3. b) Impedance values at 1 kHz, taken during culture, show that both np-Au morphologies sustain (indicating resilience to biofouling) a lower impedance than pl-Au electrodes. c) Calculated root-mean-squared (RMS) noise level is significantly lower on both np-Au morphologies than the pl-Au counterparts (error bars represent standard error of RMS noise). d) MEAs with Morphology 3 electrodes effectively coupled with more neurons in both the short and long-term time-points than both standard np-Au and pl-Au electrodes, resulting in an increased number of active electrodes through the entire recording time. e) Calculated signal-to-noise ratio (SNR) shows that both np-Au morphologies result in a higher SNR than pl-Au over all time-points, with both sustaining a higher SNR compared to pl-Au through DIV 28 (Solid lines represent median values of SNR for each DIV). f) Measured spike amplitude remains higher on both np-Au electrodes, with a shift toward Morphology 3 remaining higher at longer culture points (Solid lines represent median values of spike amplitude for each DIV).

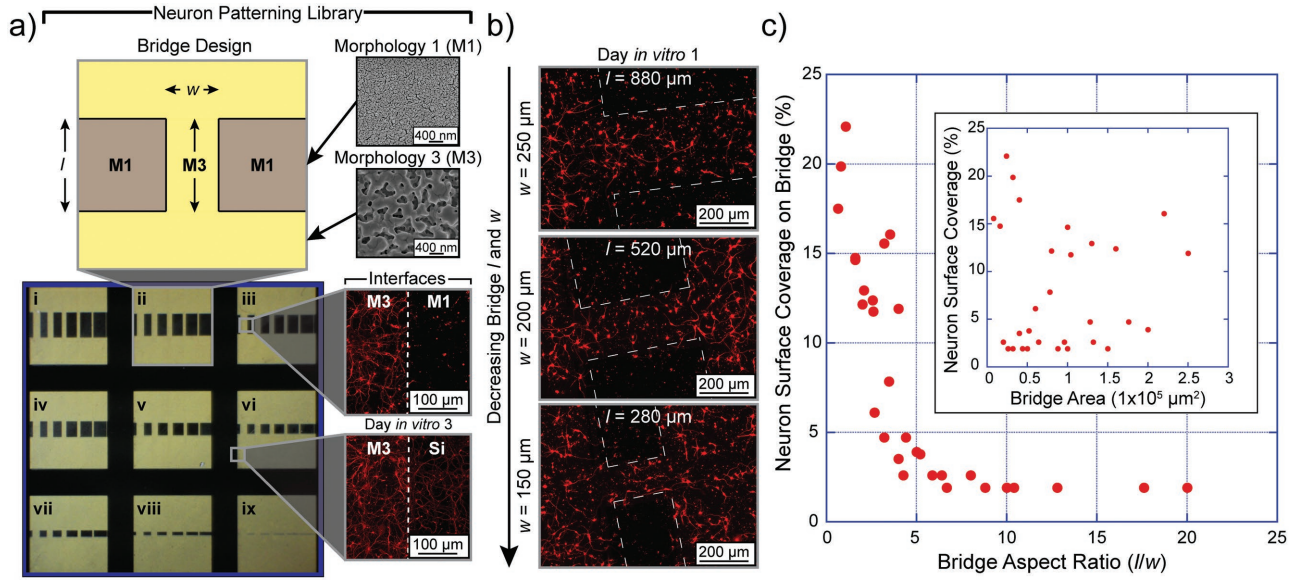

Figure 6. a) Neuron patterning libraries with laser annealed bridges were fabricated with an array of bridge widths (w) ranging from 50 to 250 μm and lengths (l) ranging from 40 to 1000 μm. Fluorescence microscopy images of tubulin-βIII immunoreactivity at the interfaces between Morphology 1 and 3 as well as Morphology 3 and silicon at DIV 3 show the sustained definition between the interfaces (white dashed line). b) Fluorescence microscopy images of tubulin-βIII immunoreactivity at DIV 1 over the bridges (outlined in white dashed lines) show preferential adherence of neurons over the laser-annealed sections. c) Surface analysis of neuron coverage over the bridges shows dependence on both bridge length and bridge width with narrower bridges requiring a shorter length for neurons to be patterned successfully (Figure S5, Supporting Information).

a higher percentage of coupled electrodes (i.e., electrodes with signals at least ten times the RMS noise level) than pl-Au, significant differences in neuron–electrode coupling stability between np-Au morphologies are seen. The percentage of active electrodes increased at all time-points for Morphology 3 electrodes, ending in ≈1.5 times the number of coupled electrodes for this morphology at DIV 28 compared to pl-Au (Figure 5d). For all the days tested, both np-Au morphologies resulted in higher signal-to-noise ratio (SNR) than were seen on the pl-Au electrodes (Figure 5e). Although some of this improvement in SNR are a result of the lowered impedance from the increased effective surface area of np-Au electrodes (as lower impedance reduces thermal noise[48]), the impedance remained constant over the entire experiment, thus, the recorded spike amplitude is the primary cause of the large changes in SNR. In fact, a similar trend is evident for the spike amplitude (Figure 5f). Initially, neurons coupled to the electrodes (judged by visible spikes) sooner for the np-Au electrodes, and the highest spike amplitudes at DIV 7 were recorded on standard np-Au. However, on all subsequent DIV, Morphology 3 electrodes demonstrated the highest spike amplitude, which remained ≈1.5 times higher than pl-Au at DIV 28. This is likely due to the effect of the large feature sizes (Figure 4) to maintain reduced astrocytic coverage and improve neuronal coverage over the duration of the experiment.

2.4. Neuronal Patterning through Precision Laser Annealing

Another direct application of nanostructure influence on neural coverage is to create *neurotrophic morphologies* using a direct laser annealing method (previously used to fabricate material feature size libraries) in order to control where neurons adhere to the substrate. This can easily be achieved because of the inhibition of neuronal cell coverage on Morphology 1 and the increase in initial neuronal cell coverage over the annealed Morphology 3. Neuron patterning libraries consisting of annealed areas (referred to as "bridges") with widths ranging from 50 to 250 μm and lengths ranging from 40 to 1000 μm were fabricated using direct laser annealing (**Figure 6**a). Cortical neuron-astrocyte co-cultures were imaged at DIV 1 to quantify the efficacy of patterned neuronal cell adhesion. As seen in Figure 6b, the initial patterning of neurons over laser-annealed bridges in the np-Au surface was achieved on many of the size ranges studied. Interestingly, the surface coverage analysis reveals a significant dependence on the bridge aspect ratio (l/w) (Figure 6c). In this analysis, we see that an aspect ratio below 5 is necessary for the successful patterning of neurons over the bridge, and the most consistent patterning is achieved when the aspect ratio is below ≈2.5. However, once the bridge length decreases to 160 μm, the specificity of neuronal coverage is significantly diminished (Figure S4, Supporting Information). Surprisingly, no correlation exists between calculated bridge surface area and neuron surface coverage over the bridges (Figure 6c inset). This suggests that successful neuronal patterning over the bridges is governed in part by another mechanism, such as cell-to-cell interactions, that is strongly influenced by the aspect ratio (i.e., proximity to larger cell populations) and not simply the surface area available for cellular attachment.

This ability for np-Au interfaces to achieve improved long-term neural coupling and specifically pattern neuronal adhesion identifies np-Au as a unique multifunctional surface that demonstrates the potential to design custom recording sites that will significantly increase signal fidelity for recording electrodes.

3. Conclusion

In conclusion, we have demonstrated that the cell type-specific surface coverage observed on np-Au surfaces with small (≈30 nm) feature sizes is mediated through the inhibition of focal adhesion formation on the material nanostructure, whereas on large (≈170 nm and greater) feature sizes, the differential coverage is likely achieved through a different mechanism. A comprehensive analysis of astrocyte focal adhesion properties on multiple np-Au feature sizes and unstructured pl-Au revealed that focal adhesion formation is modulated by the np-Au surface feature size. We demonstrated that np-Au with small feature sizes causes a significant increase in focal adhesion number while decreasing the average focal adhesion contact area. It is plausible that the inability of astrocytes to successfully form large focal adhesion complexes on the nanostructured surface contributes to the decreased astrocyte coverage on these surfaces. Although np-Au with larger feature sizes caused a sustained reduction in astrocytic surface coverage, focal adhesion formation was marked only by a significant decrease in total focal adhesion contact area, contrary to the trend seen in the smaller feature sizes. This points toward a mechanism other than inhibition of focal adhesion formation driving the differential coverage seen on np-Au with large feature sizes. While all feature sizes tested reduced astrocytic surface coverage to DIV 7 (in comparison to silicon and pl-Au), analysis of neuronal surface coverage on the various np-Au feature sizes revealed faster initial neuronal surface coverage on np-Au with large feature sizes. To investigate the effect of this response on electrophysiological recording properties, multiple electrode arrays with both standard np-Au and Morphology 3 electrode surfaces were fabricated. Both standard np-Au and Morphology 3 resulted in improved electrode performance (i.e., higher SNR due to lower noise and higher spike amplitude). However, the effect of increased initial neuronal surface coverage on large feature sizes manifested itself through increased electrode coupling and both short- and long-term gains in electrophysiological recording performance. This indicates that utilizing nanostructured surfaces may enhance the chronic stability of neuron–electrode coupling by reducing gliosis around recording sites. Additionally, utilizing laser-annealed patterns, the specific adherence of neurons was achieved, and we demonstrated that both pattern width and length are important for the successful patterning of neurons. Ultimately, we show the ability to tune astrocytic focal adhesion formation through np-Au feature size and simultaneously pattern neuronal cell adherence. This effect, coupled with high effective surface area,[49] anti-biofouling properties,[46] low electrical impedance, and tunable drug release,[50,51] identifies np-Au as a unique multifunctional neural interface material that can both mechanically and chemically control cell response to enhance long-term electrophysiological recording performance.

4. Experimental Section

General Sample Fabrication: The non-material library based samples used in this study were deposited in 5 mm diameter spots onto piranha-cleaned 12 mm diameter glass slides (0.15 mm thick, TedPella) using laser cut polydimethylsiloxane (PDMS) films as a stencil mask. Unstructured gold (pl-Au) samples were deposited by direct current sputtering (Kurt J. Lesker) of a 160 nm thick chromium adhesion layer and subsequently a 200 nm thick gold layer. Gold-silver alloy samples were fabricated by the sequential sputtering of a 160 nm chromium adhesion layer, 80 nm gold corrosion barrier layer, and the co-sputtering of a 600 nm thick gold and silver alloy (64% silver and 36% gold; atomic (at) %). The final np-Au films were produced by immersing the gold-silver alloy in heated (55 °C) nitric acid (70%) for 15 min, a process known as dealloying. The dealloyed samples were then soaked in deionized (DI) water for one week while changing the water every 24 h.

Material Library Sample Fabrication: The material libraries of np-Au were first patterned into an array consisting of nine 3 × 3 mm squares through traditional photolithography, deposition, and lift-off stages (all performed at the Center for Nano and Micro-machining at the University of California, Davis). In brief, 500 µm thick silicon wafers (University Wafer) were spun with ≈2 µm of AZ 5214E-IR (Clariant) and patterned using a film mask. Alloy deposition was then carried out as per the previously mentioned protocol. After deposition, the lift-off process was completed through 4 h exposure to *N*-methyl-2-pyrrolidone (NMP). After lift-off each chip was diced from the wafer and dealloyed using the previously mentioned protocol. These dealloyed chips were then stored in DI water for one week while changing water every 24 h. After drying each chip was photothermally annealed using a custom 532 nm continuous-wave laser as reported previously.[29] Using laser powers of 1000 and 750 mW, libraries consisting of heavily annealed, slightly annealed, and unannealed morphologies were created.

Sample Characterization: The morphologies of all np-Au films produced in this study were characterized through the analysis of scanning electron microscopy images (FEI Nova Nano-SEM430). Feature size analysis was performed using custom ImageJ, MATLAB, and Python scripts to determine film ligament width and pore sizes. All ligament width and pore areas in this paper are represented by an average value plus or minus the standard error. Additionally, the elemental composition of each film before and after dealloying was assessed through energy dispersive X-ray spectroscopy (Oxford INCA, Energy-EDS).

General Cell Culture: Primary rat cortical cells were obtained from perinatal (day 0) Sprague-Dawley rats from the laboratory of Prof. Pamela J. Lein at the University of California, Davis.[52] All studies were conducted according to protocols approved by the Institutional Animal Care and Use Committee of the University of California, Davis. Before plating, surfaces were pre-coated with 0.5 mg mL^{-1} of poly-L-lysine in B buffer (3.1 mg mL^{-1} boric acid and 4.75 mg mL^{-1} borax, Sigma) at 37 °C and 5% CO_2 for 4 h. All samples were then washed with sterile deionized water before being soaked in plating media (Neurobasal A culture medium supplemented with 2% B27 supplement, 10% heat inactivated horse serum, 1× Glutamax, and 1 M HEPES at pH 7.5—all ThermoFisher) for 12 h at 37 °C and 5% CO_2. Dissociated cortical cells were plated onto the samples at a density of ≈520 cells mm^{-2} and kept in plating media to attach to the substrate. After 4 h, cultures were switched to a serum-free growth media (neurobasal medium supplemented with 2% B27 supplement) and incubated at 37 °C and 5% CO_2. Growth media was replenished at DIV 3 and 7.

Immunocytochemistry: Cultures were fixed using 4% paraformaldehyde (Affymetrix). Fixed cultures were then stained using Alexa Fluor pre-conjugated phalloidin (1:500) and anti-vinculin primary antibodies (1:100) to visualize cytoskeleton and focal adhesions, respectively, the latter being visualized using Alexa Fluor conjugated secondary antibodies (1:100). In order to visualize neuron and astrocytic surface coverage, cells were immunostained with anti-tubulin-βIII (1:100) and anti-GFAP (1:100), respectively. All samples were counter-stained with a DAPI nuclear stain to quantify cell number. All antibodies were purchased from ThermoFisher Scientific.

Cell SEM Preparation: For scanning electron microscopy, cultures were fixed using 2.5% glutaraldehyde (Sigma). Fixed cells were then dried using a cascaded exchange of lower surface energy liquids from PBS to absolute ethanol to hexamethyldisilizane (HMDS) (Sigma). The

HMDS was allowed to evaporate under a fume hood exposing the dry fixed cells. A thin 2.5 nm thick gold layer was then sputtered onto the sample surface to allow scanning electron microscopy imaging.

Multiple Electrode Array Fabrication and Electrophysiological Recordings: Sputtered Cr-Au-Ti traces (20 nm thick Cr, 100 nm thick Au, and 30 nm thick Ti) were defined on a glass wafer (University Wafers) by lift-off procedure with image reversal photoresist AZ5214E (Clariant). A 2.5 µm thick AZ5214E layer was made by lithography to define electrode openings in the insulation layer. A 550 nm silicon nitride layer was deposited as insulator by RF reactive sputtering in 2.5 mTorr Ar:N_2 gas mixture (34:17 sccm) with Si target at 300 W for 6 h. After lift-off in NMP, the substrates were soaked in chromium etchant 1020AC for 30 s to expose the Au surface at the electrode openings. Another 2.5 µm thick AZ5214E layer was used to define the AuAg alloy layer on selected recording sites. After alloy sputtering (using the previously mentioned settings) and lift-off procedure, the substrates were diced and dealloyed. MEAs were soaked in DI water for 7 d before use. There are thirty-two 20 µm diameter recording sites on each MEA. 24 of them are covered by 500–600 nm thick nanoporous gold film. Additionally, eight of them are pure gold surfaces that are randomly distributed in the 8×4 electrode array to avoid location bias in electrophysiology recording test. To achieve a heavily annealed morphology, MEAs were annealed using rapid thermal processing (RTP) at 300 °C under a nitrogen environment for a total of 6 min.

Before starting the neural culture, MEAs were mounted with sterile glass cloning cylinders (Sigma) using sterile silicon grease as a sealant. In order to reduce evaporation of the small media volume sterile PET film was mounted on top of the cloning cylinder using silicon grease as a sealant. Primary cortical cultures were grown as stated above, with the exception that only half media changes once per week were performed during the culture time. 2 h recordings and impedance values were taken at days in vitro 7, 14, and every subsequent day until 28 from both the unannealed MEA and the annealed MEA. Recordings were performed at a sampling rate of (30 kS s^{-1}) with a custom rig connecting the MEAs to an (RHD2132) Intan amplifier (Intan Technologies). The electrophysiological data were analyzed using a modified version of the Wave_Clus[53] MATLAB program.

Statistical Methods: Each study was performed with a sample size of three samples per dissection and imaged in at least three locations on the sample. Studies involving material libraries were performed with an internal sample size of three repeats per np-Au morphology. Only one material library was used per dissection. All reported values are averages with error bars corresponding to the standard deviation of each averaged data set unless otherwise noted. A two-tailed Student's *t*-test assuming unequal variance was used to identify differences between two different sample groups. Unless otherwise noted, a one-way ANOVA was used when comparing more than one group of samples. Statistical significant was determined by *p*-values < 0.05.

Supporting Information

Supporting Information is available from the Wiley Online Library or from the author.

Acknowledgements

The authors gratefully acknowledge support from UC Lab Fees Research Program Award [12-LR-237197], Research Investments in the Sciences and Engineering (RISE) Award, National Science Foundation Grants [CBET-1512745 and CBET&DMR-1454426], and UC Davis College of Engineering start-up funds. C. A. R. Chapman was supported by a National Science Foundation Graduate Research Fellowship [DGE-1650042]. Support was also provided by the CounterACT Program, National Institutes of Health Office of the Director and the National Institute of Neurological Disorders and Stroke [U54 NS079202]. H. Chen was supported by a predoctoral fellowship from the National Institute of Environmental Health Sciences [T32 ES007059] and received a predoctoral fellowship from the Superfund Basic Research Program [P42 ES04699]. The authors would also like to extend a special thanks to the collaborators at Lawrence Livermore National Laboratory, Dr. Manyalibo Matthews, Dr. Monika Biener, and Dr. Juergen Biener who have helped in building the laser annealing system and relocating it to UC Davis.

Received: September 6, 2016
Published online: December 12, 2016

[1] A. Leal-Egaña, A. Díaz-Cuenca, A. R. Boccaccini, *Adv. Mater.* **2013**, *25*, 4049.
[2] M. Schvartzman, M. Palma, J. Sable, J. Abramson, X. Hu, M. P. Sheetz, S. J. Wind, *Nano Lett.* **2011**, *11*, 1306.
[3] J. P. Spatz, B. Geiger, *Methods Cell Biol.* **2007**, *83*, 89.
[4] V. Vogel, M. Sheetz, *Nat. Rev. Mol. Cell Biol.* **2006**, *7*, 265.
[5] M. J. Dalby, G. E. Marshall, H. J. H. Johnstone, S. Affrossman, M. O. Riehle, *IEEE Trans. Nanobiosci.* **2002**, *1*, 18.
[6] M. J. P. Biggs, R. G. Richards, M. J. Dalby, *Nanomedicine* **2010**, *6*, 619.
[7] P. Vandrangi, S. C. Gott, R. Kozaka, V. G. J. Rodgers, M. P. Rao, *PLoS ONE* **2014**, *9*, e111465.
[8] B. K. K. Teo, S. T. Wong, C. K. Lim, T. Y. S. Kung, C. H. Yap, Y. Ramagopal, L. H. Romer, E. K. F. Yim, *ACS Nano* **2013**, *7*, 4785.
[9] K. Yang, K. Jung, E. Ko, J. Kim, K. I. Park, J. Kim, S.-W. Cho, *ACS Appl. Mater. Interfaces* **2013**, *5*, 10529.
[10] E. K. F. Yim, E. M. Darling, K. Kulangara, F. Guilak, K. W. Leong, *Biomaterials* **2010**, *31*, 1299.
[11] A. Ferrari, M. Cecchini, M. Serresi, P. Faraci, D. Pisignano, F. Beltram, *Biomaterials* **2010**, *31*, 4682.
[12] E. S. Ereifej, H. W. Matthew, G. Newaz, A. Mukhopadhyay, G. Auner, I. Salakhutdinov, P. J. VandeVord, *J. Biomed. Mater. Res., A* **2013**, *101*, 1743.
[13] V. Brunetti, G. Maiorano, L. Rizzello, B. Sorce, S. Sabella, R. Cingolani, P. P. Pompa, *Proc. Natl. Acad. Sci. USA* **2010**, *107*, 6264.
[14] Y. H. Tan, S. E. Terrill, G. S. Paranjape, K. J. Stine, M. R. Nichols, *Biomater. Sci.* **2014**, *2*, 110.
[15] A. J. Woolley, H. A. Desai, K. J. Otto, *J. Neural Eng.* **2013**, *10*, 026007.
[16] E. S. Ereifej, S. Khan, G. Newaz, J. Zhang, G. W. Auner, P. J. VandeVord, *J. Biomed. Mater. Res., A* **2011**, *99A*, 141.
[17] V. S. Polikov, P. A. Tresco, W. M. Reichert, *J. Neurosci. Methods* **2005**, *148*, 1.
[18] B. Ilic, D. Czaplewski, P. Neuzil, T. Stanczyk, J. Blough, G. J. Maclay, *J. Mater. Sci.* **2000**, *35*, 3447.
[19] D. Brüggemann, K. E. Michael, B. Wolfrum, A. Offenhäusser, *Int. J. Nano Biomater.* **2012**, *4*, 108.
[20] X. Cui, J. F. Hetke, J. A. Wiler, D. J. Anderson, D. C. Martin, *Sens. Actuators, A* **2001**, *93*, 8.
[21] K. Wang, H. A. Fishman, H. Dai, J. S. Harris, *Nano Lett.* **2006**, *6*, 2043.
[22] T. J. Webster, M. C. Waid, J. L. McKenzie, R. L. Price, J. U. Ejiofor, *Nanotechnology* **2003**, *15*, 48.
[23] S. F. Cogan, *Annu. Rev. Biomed. Eng.* **2008**, *10*, 275.
[24] N. A. Kotov, J. O. Winter, I. P. Clements, E. Jan, B. P. Timko, S. Campidelli, S. Pathak, A. Mazzatenta, C. M. Lieber, M. Prato, R. V. Bellamkonda, G. A. Silva, N. W. S. Kam, F. Patolsky, L. Ballerini, *Adv. Mater.* **2009**, *21*, 3970.
[25] E. Seker, Y. Berdichevsky, M. R. Begley, M. L. Reed, K. J. Staley, M. L. Yarmush, *Nanotechnology* **2010**, *21*, 125504.

[26] Y. H. Kim, G. H. Kim, A. Y. Kim, Y. H. Han, M.-A. Chung, S.-D. Jung, *J. Neural Eng.* **2015**, *12*, 066029.
[27] C. A. R. Chapman, H. Chen, M. Stamou, J. Biener, M. M. Biener, P. J. Lein, E. Seker, *ACS Appl. Mater. Interfaces* **2015**, *7*, 7093.
[28] J. Erlebacher, M. J. Aziz, A. Karma, N. Dimitrov, K. Sieradzki, *Nature* **2001**, *410*, 450.
[29] C. A. R. Chapman, L. Wang, J. Biener, E. Seker, M. M. Biener, M. J. Matthews, *Nanoscale* **2015**, *8*, 785.
[30] M. V. Sofroniew, H. V. Vinters, *Acta Neuropathol.* **2010**, *119*, 7.
[31] J. D. Humphries, P. Wang, C. Streuli, B. Geiger, M. J. Humphries, C. Ballestrem, *J. Cell Biol.* **2007**, *179*, 1043.
[32] R. M. Ezzell, W. H. Goldmann, N. Wang, N. Parashurama, N. Parasharama, D. E. Ingber, *Exp. Cell Res.* **1997**, *231*, 14.
[33] N. R. Blumenthal, O. Hermanson, B. Heimrich, V. P. Shastri, *Proc. Natl. Acad. Sci. USA* **2014**, *111*, 16124.
[34] J. Z. Gasiorowski, S. J. Liliensiek, P. Russell, D. A. Stephan, P. F. Nealey, C. J. Murphy, *Biomaterials* **2010**, *31*, 8882.
[35] D.-H. Kim, D. Wirtz, *FASEB J.* **2013**, *27*, 1351.
[36] D.-H. Kim, D. Wirtz, *Cell Adhes. Migr.* **2013**, *7*, 293.
[37] S. R. Coyer, A. Singh, D. W. Dumbauld, D. A. Calderwood, S. W. Craig, E. Delamarche, A. J. García, *J. Cell Sci.* **2012**, *125*, 5110.
[38] E. A. Cavalcanti-Adam, A. Micoulet, J. Blummel, J. Auernheimer, H. Kessler, J. P. Spatz, *Eur. J. Cell Biol.* **2006**, *85*, 219.
[39] N. Tawil, P. Wilson, S. Carbonetto, *J. Cell Biol.* **1993**, *120*, 261.
[40] C. O. Arregui, S. Carbonetto, L. McKerracher, *J. Neurosci.* **1994**, *14*, 6967.
[41] L. M. Y. Yu, N. D. Leipzig, M. S. Shoichet, *Mater. Today* **2008**, *11*, 36.
[42] B. Geiger, J. P. Spatz, A. D. Bershadsky, *Nat. Rev. Mol. Cell Biol.* **2009**, *10*, 21.
[43] A. Kamkin, I. Kiseleva, *Mechanosensitivity and Mechanotransduction* (Eds: A. Kamkin, I. Kiseleva), Springer, Dordrecht, The Netherlands **2011**.
[44] N. Arimura, K. Kaibuchi, *Nat. Rev. Neurosci.* **2007**, *8*, 194.
[45] N. D. Gallant, K. E. Michael, A. J. García, *Mol. Biol. Cell* **2005**, *16*, 4329.
[46] P. Daggumati, Z. Matharu, L. Wang, E. Seker, *Anal. Chem.* **2015**, *87*, 8618.
[47] J. Patel, L. Radhakrishnan, B. Zhao, B. Uppalapati, R. C. Daniels, K. R. Ward, M. M. Collinson, *Anal. Chem.* **2013**, *85*, 11610.
[48] D. A. Robinson, *Proc. IEEE* **1968**, *56*, 1065.
[49] E. Seker, M. Reed, M. Begley, *Materials* **2009**, *2*, 2188.
[50] O. Kurtulus, P. Daggumati, E. Seker, *Nanoscale* **2014**, *6*, 7062.
[51] S. D. Gittard, B. E. Pierson, C. M. Ha, C.-A. M. Wu, R. J. Narayan, D. B. Robinson, *Biotechnol. J.* **2010**, *5*, 192.
[52] G. A. Wayman, S. Impey, D. Marks, T. Saneyoshi, W. F. Grant, V. Derkach, T. R. Soderling, *Neuron* **2006**, *50*, 897.
[53] R. Q. Quiroga, Z. Nadasdy, Y. Ben-Shaul, *Neural Comput.* **2004**, *16*, 1661.